15 GHz SPACE VLBI OBSERVATIONS USING AN ANTENNA ON A TDRSS SATELLITE

R. P. LINFIELD, G. S. LEVY, C. D. EDWARDS, AND J. S. ULVESTAD
Jet Propulsion Laboratory, California Institute of Technology

C. H. OTTENHOFF
TRW Space and Technology Group

H. HIRABAYASHI,[1] M. MORIMOTO, AND M. INOUE
Nobeyama Radio Observatory

D. L. JAUNCEY
Commonwealth Scientific and Industrial Organization

J. REYNOLDS
Australian National University

T. NISHIMURA, T. HAYASHI, T. TAKANO, AND T. YAMADA
Institute for Space and Astronautical Science

J. W. BARRETT, S. R. CONNER, M. B. HEFLIN, J. LÉHAR, AND B. F. BURKE
Massachusetts Institute of Technology

D. H. ROBERTS
Brandeis University

A. R. WHITNEY, R. J. CAPPALLO, AND A. E. E. ROGERS
Haystack Observatory

M. W. POSPIESZALSKI
National Radio Astronomy Observatory

S. J. DINARDO, L. J. SKJERVE, AND L. R. STAVERT
Jet Propulsion Laboratory, California Institute of Technology

AND

M. J. MAHER
Bendix Field Engineering Corporation

ABSTRACT

A 4.9 m diameter antenna in earth orbit, part of the Tracking and Data Relay Satellite System, was previously used for space VLBI observations at 2.3 GHz. It has now been used successfully with two ground antennas for VLBI measurements at 15 GHz. Although the sensitivity (gain/system temperature) of the orbiting antenna was a factor of 6 poorer at 15 GHz than at 2.3 GHz, 11 out of 22 extragalactic sources were detected on space-ground baselines, up to a maximum baseline of 1.63 Earth diameters. The results suggest that the distribution of source visibilities at 15 and 2.3 GHz are similar for these baseline lengths. Model-dependent brightness temperatures of $1-2.5 \times 10^{12}$ K were derived for six sources. This suggests that sources with brightness temperatures in this range are as common at 15 GHz as at 2.3 GHz. The coherence on space-ground baselines (This includes effects due to the phase transfer from the ground to the satellite and the reconstruction of the spacecraft orbit) was 0.76 for 340 s integrations. A small number of VLBI data at 2.3 GHz were also obtained.

Subject headings: instruments — interferometry — radio sources: galaxies

I. INTRODUCTION

The highest angular resolution of any current astronomical observational technique results from very long baseline interferometry (VLBI) at radio frequencies (Broten *et al.* 1967). The resolution of VLBI is limited only by the observing frequency and baseline length. With global ground arrays, resolutions of the order of 1 milliarcsecond (mas) can be achieved at centimeter wavelengths, and a factor of 10 smaller in the millimeter region. However, even with baseline lengths of nearly an Earth

diameter, many sources are only slightly resolved, independent of observing wavelength.

A radio telescope in space can greatly improve the resolution of current VLBI arrays. The most suitable existing satellites for VLBI observations are those of the tracking and data relay satellite system (TDRSS) (Sade and Deerkoski 1981). Although the geostationary orbits of these satellites are not optimal for VLBI imaging, the satellite oscillator chains are suitable for VLBI. There are currently two approved projects to place a telescope in earth orbit specifically for VLBI purposes: VSOP by the Institute for Space and Astronautical Science in Japan (Hirabayashi 1987), and RADIOASTRON by

---

[1] Currently at Institute for Space and Astronautical Science.

350

the Space Research Institute of the USSR Academy of Science (Kardashev and Slysh 1987). Both projects plan launches in the 1993–1995 time period.

In 1986 July–August and 1987 January (hereafter referred to as the first and second experiments, respectively), the first satellite in the TDRSS system, *TDRSA*, was used for VLBI observations at 2.3 GHz. (The term "*TDRSE*" used in earlier papers referred to the positioning of the satellite in the "eastern" orbit. With multiple satellites now in orbit, we have chosen to refer to the satellite, not the orbit.) These observations (Levy *et al.* 1986, 1989) demonstrated several technical capabilities required for space VLBI. These capabilities include: phase transfer from a ground frequency standard to a local oscillator on the satellite, transfer of intermediate-frequency (IF) data from the orbiting antenna to the ground for recording, and the use of satellite orbit information in data correlation. Sources were detected on baselines as long as 2.15 Earth diameters, directly demonstrating the existence of brightness temperatures in the range $1-4 \times 10^{12}$ K in extragalactic continuum sources (Linfield *et al.* 1989).

Each of the two 4.9 m diameter antennas on a TDRSS satellite has receivers at two frequencies: 2.3 and 15 GHz. The coherence requirements for space VLBI at 15 GHz are much more stringent than at 2.3 GHz, especially in the demands placed on knowledge of the satellite orbit (errors in orbit knowledge cause a coherence loss approximately proportional to the square of the observing frequency). In an effort to determine at what level these requirements could be met, 15 GHz VLBI observations were conducted with *TDRSA* in 1988 February and March. A second goal of this experiment was to perform a space VLBI survey at a higher observing frequency than 2.3 GHz.

II. OBSERVATIONS

The experimental procedure was similar to that used at 2.3 GHz (Levy *et al.* 1989). The same satellite, *TDRSA*, in geostationary orbit over 41° west longitude, was used. This satellite was controlled from the White Sands Ground Terminal

(WSGT) in New Mexico. The uplink in the 15 GHz band and the downlink in the 13.5 GHz band used the 2.0 m diameter space-to-ground link antenna on board the spacecraft. A drawing of the spacecraft was presented in Levy *et al.* (1989). A block diagram of the TDRSS observing system is shown in Figure 1.

Simultaneous observations at 2.3 and 15 GHz were performed, using coaxial feeds on the same 4.9 m antenna on *TDRSA*. Two ground antennas were used for the 15 GHz observations: a 70 m diameter antenna (DSS 43) of the NASA Deep Space Network in Tidbinbilla, Australia and a 45 m diameter antenna of the Nobeyama Radio Observatory (NRO) in Japan. The ground observations at 2.3 GHz were less complete. Of the seven observing sessions, a 34 m diameter DSN antenna (DSS 42) in Tidbinbilla, Australia was used for $1\frac{1}{2}$ sessions. The 64 m diameter antenna (Usuda) of the Institute for Space and Astronautical Science in Usuda, Japan was used for six of the seven sessions. However, technical problems at Usuda allowed valid data to be obtained only for the last two sessions. A summary of observing dates and ground arrays is given in Table 1.

TDRSA used uncooled transistor receivers at both 15 and 2.3 GHz. DSS 43 used a cooled 15 GHz FET receiver loaned by the National Radio Astronomy Observatory (NRAO). NRO used a copy of the NRAO receiver built at the Massachusetts Institute of Technology. Despite the identical designs of the receivers at NRO and DSS 43, the total system temperature at NRO was substantially larger than at DSS 43. The reason for this is not known. The combination of higher system temperature and smaller aperture size of NRO (compared to DSS 43) resulted in a factor of 1.7 lower sensitivity on the *TDRSA*–NRO baseline than on the *TDRSA*–DSS 43 baseline. The "sensitivity" is defined as the ratio of antenna temperature to system temperature for a source of unit flux density. DSS 42 used a maser receiver, and Usuda used a cooled parametric amplifier. The system temperatures and apertures of the receiving systems are given in Table 2.

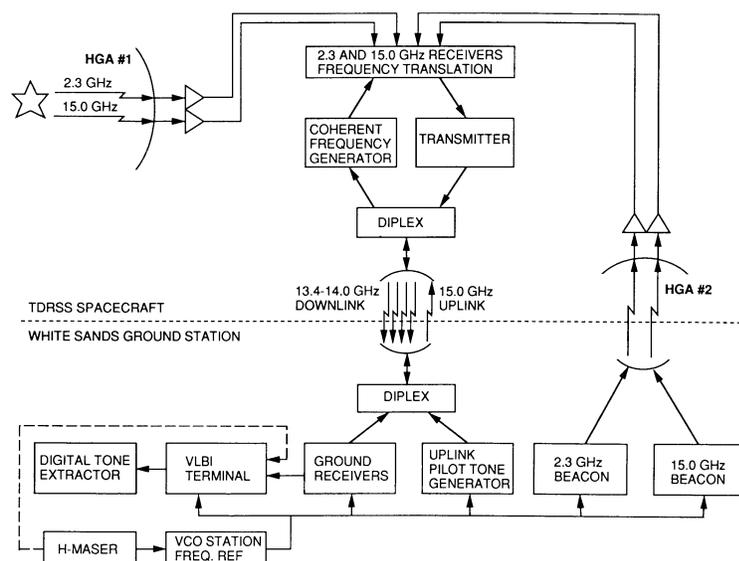IF data from all antennas were digitized and recorded with

Fig. 1.—Block diagram of the TDRSS 15 GHz observing system used in this experiment. The dashed line indicates the signal path used for calibration of the hydrogen maser during the last two observing sessions.

TABLE 1

OBSERVING DATES AND GROUND ARRAYS

Session	Date (1988)	Duration (hr)	15 GHz Ground Array	2.3 GHz Ground Array
1................	Feb 4	4	DSS 43	Usuda[a]
2................	Feb 7	4	DSS 43, NRO	DSS 42, Usuda[a]
3[b].............	Feb 23	3.5	DSS 43, NRO	Usuda[a]
4................	Feb 25	5.7	DSS 43, NRO	DSS 42[c], Usuda[a]
5................	Feb 27–28	4	DSS 43, NRO	...
6................	Mar 6	4	DSS 43, NRO	Usuda
7................	Mar 10	4	DSS 43, NRO	Usuda

[a] No usable data were obtained from Usuda during sessions 1–4.

[b] No fringes on space-ground baselines were detected during session 3.

[c] DSS 42 observed for only 1.5 hr during this session.

the Mark III (Mk III) VLBI recording system (Rogers *et al.* 1983), using channels of 4 MHz bandwidth. The IF data from *TDRSA* were broadcast to the ground before being filtered into channels, digitized, and time-tagged. Twenty-two channels of 15 GHz data (total bandwidth of 88 MHz) were recorded in a single 400 s pass on each Mk III tape at WSGT, Tidbinbilla, and NRO. Three channels of 2.3 GHz data (total bandwidth of 12 MHz) were recorded at WSGT, Tidbinbilla, and Usuda. At WSGT and Tidbinbilla, the 15 and 2.3 GHz data were recorded on the same tape. The combined 2.3 and 15 GHz bandwidth (100 MHz) was less than the maximum Mk III double-speed bandwidth of 112 MHz. This sacrifice of bandwidth was necessary due to operational constraints of the Haystack correlator in processing the one-pass-per-tape WSGT 2.3 GHz data with the four-passes-per-tape Usuda data (this recording mode was used at Usuda in order to reduce tape usage). The 2.3 GHz bandwidth of 12 MHz was nearly the maximum allowed by the *TDRSA* passband of 16 MHz. The 15 GHz bandwidth of 88 MHz was considerably less than the *TDRSA* passband of 256 MHz and was limited entirely by the Mk III recording and correlating capability.

The WSGT–*TDRSA* phase transfer operates as a one-way link. In order to calibrate the phase of this link, the capability of a round trip phase measurement had to be added (Levy *et al.* 1989). A beacon was transmitted from WSGT to the spacecraft, where it was received with one of the 4.9 m antennas, amplified, frequency-translated, and transmitted back to WSGT. There its phase was compared to the phase of the frequency standard used to generate the beacon, using a digital phase-locked loop. In the first two experiments, a single beacon at 2.3 GHz was used, with a phase measurement every 2 s. In this experiment, beacons at both 2.3 and 15 GHz were used, with the phase of each one measured every 3 s. The residuals to a cubic polynomial fit for 400 s of data were of similar magnitude (1–5 ps) for the two beacons. The phases of the two beacons had a relative coherence exceeding 90% for 600 s. Both 2.3 and 15 GHz link delay measurements exhibited substantially smaller residuals (by factors of 2–3) than did the 2.3 GHz measurements in the first two experiments, for unknown reasons.

In the first two experiments, WSGT used a cesium frequency standard to generate the local oscillator (LO) uplink for *TDRSA*. To improve upon the frequency stability of the Cs standard over the 800 s scans, the phase of this standard was compared to that of a hydrogen maser during the observations, with phase-correction of the data performed later at the correlator (Levy *et al.* 1989). For the third experiment, a hydrogen maser was used as the primary frequency standard at WSGT.

This was intended to provide superior phase purity without the need for subsequent correction. However, the maser was not optimally configured at WSGT. On time scales greater than about 1 s, a hydrogen maser exhibits superior phase purity to a crystal oscillator. For time scales shorter than about 1 s, the reverse is true. In most VLBI experiments in which a hydrogen maser is used, the maser is connected to a crystal oscillator "flywheel" using a phase-lock loop with a time constant of approximately 1 s. This configuration combines the superior short-term stability of the crystal with the long-term stability of the maser. In the third experiment, a 100 s time constant was used in the phase-lock loop. This caused the resulting coherence to be substantially worse than that of the maser on time scales up to 200–300 s. This misconfiguration was discovered after the fifth observing session, but due to operational constraints at WSGT, it could not be changed. However, real time phase comparisons between the raw maser output and the "corrupted" maser output were made during all of the sixth and seventh sessions (indicated by the dashed line in Fig. 1). This comparison was done in the same way that comparisons between a hydrogen maser and cesium oscillator were made during the first two experiments. The observed phase differences were used to improve the coherence for the last two sessions during fringe-fitting at the correlator. The coherence with and without these corrections is presented in § IV.

The pointing restrictions on *TDRSA* were less severe than in the previous experiments and were set by the hardware limits of the 4.9 m antenna which was observing the radio source. These limits consisted of the interior of an ellipse centered on the nadir, with semimajor axis (in declination) of 31° and semiminor axis (in hour angle) of 22°. The region north of +14° declination was inaccessible, as was the earth occultation region of approximately 9° radius, centered on the nadir (Fig. 2).

The large orbit of *TDRSA* and the narrow hour angle limits caused the *TDRSA*–Japan and *TDRSA*–Australia u-v tracks to be nearly straight lines, parallel to the u-axis. Their separation was approximately $R_\oplus (\sin \phi_J - \sin \phi_A) \cos \delta$, where $R_\oplus$ is the radius of the Earth, ϕ_J is the latitude of the Japanese telescope, ϕ_A is the latitude of the Australian telescope ($\phi_J \approx -\phi_A$), and δ is the source declination.

Due to the low sensitivity expected for space-ground baselines, the source selection was based entirely on the expected correlated flux densities. VLBI surveys on intercontinental baselines at 2.3 GHz and 8.4 GHz (Morabito *et al.* 1986) were used to predict (by linear extrapolation) 15 GHz correlated flux densities on 8000–10,000 km baselines. Those sources in

TABLE 2

PARAMETERS OF THE TELESCOPES USED FOR THIS EXPERIMENT

Antenna	Diameter (m)	Observing Frequency (GHz)	Total Off-Source System Temperature (Zenith) (K)	Recorded Bandwidth (MHz)	Latitude	Longitude
TDRSA	4.9	15	1000	88	...	...
		2.3	300	12	...	...
DSS 43	70	15	50	88	35°.2 S	149°.0 E
NRO	45	15	80	88	35°.9 N	138°.5 E
DSS 42	34	2.3	16	12	35°.2 S	149°.0 E
Usuda	64	2.3	30	12	36°.1 N	138°.4 E

the (−31°, +14°) declination range with the largest predicted 15 GHz correlated flux densities were observed. Although simultaneous 2.3 GHz observations were conducted, the source selection criteria were based entirely upon expected 15 GHz properties.

III. DATA REDUCTION

Correlation of the data was performed with the Mark IIIA correlator at Haystack Observatory, as in the first two experiments. The *TDRSA* orbit ephemeris was produced at Goddard Space Flight Center, reprocessed at the Jet Propulsion Laboratory, and used in the correlator model in the same way as described in Levy *et al.* (1989). Residual phase values from the

link calibration were used to correct the data during the fringe-fitting process. Due to the relatively small residual link phases measured during this experiment, this correction produced only a minor improvement to the coherence. For sessions 6 and 7, phase measurements of the corrupted WSGT hydrogen maser were available, and were applied during fringe-fitting.

For three sources (1334−127, 1510−089, and 1730−130) observed in sessions 1–5 (when the coherence on baselines to *TDRSA* was poor because of the equipment configuration at WSGT), a phase correction technique was used to reduce the detection threshold on the *TDRSA*–NRO baseline by a factor of ≈2 (from 1.5 to 0.7–0.8 Jy). For these three sources, the projected length of the *TDRSA*–NRO baseline was approx-
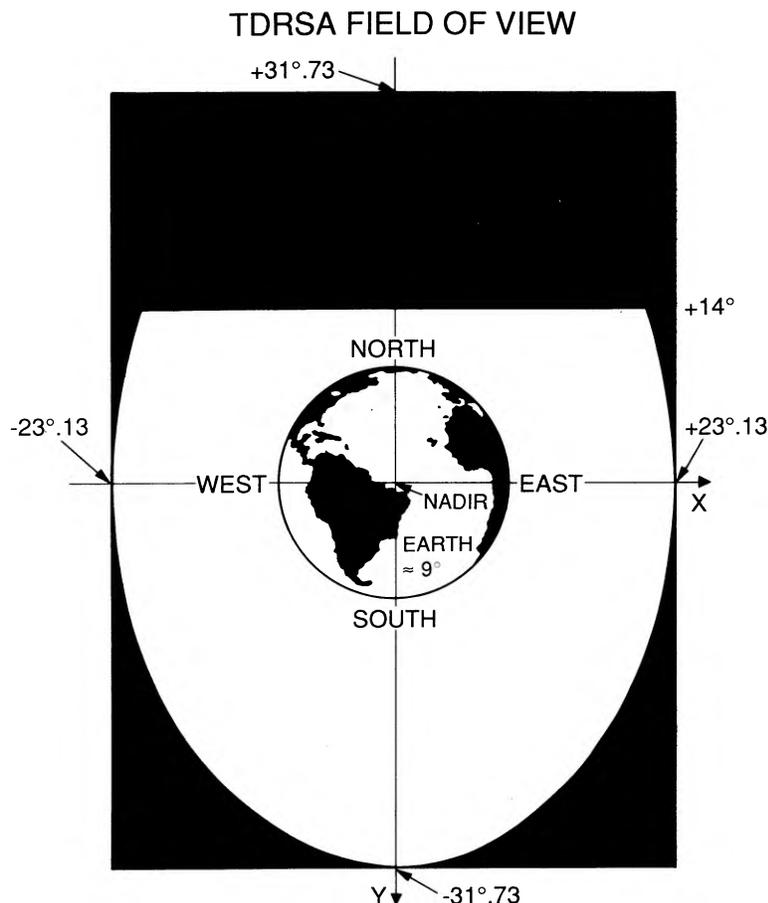
TDRSA FIELD OF VIEW

FIG. 2.—Field of view of *TDRSA* (drawn to scale) in this experiment. The declination range is (−31°, +14°) and the hour angle range is (−22°, +22°). The region around the nadir is occulted by the Earth.

imately twice the projected length of the *TDRSA*–DSS 43 baseline. The signal-to-noise ratios (S/N's) of these sources on the *TDRSA*–DSS 43 baseline were substantially larger than on the *TDRSA*–NRO baseline and were among the largest obtained in this experiment. Fringe-fitting with short integration times on the *TDRSA*–DSS 43 baseline allowed a measurement of the *TDRSA* phase on time scales as short as 10 s (limited by S/N). These measurements were used to rotate the phases on the *TDRSA*–NRO baseline and to correct for much of the coherence loss on time scales greater than 10 s. The effective coherence on the *TDRSA*–NRO baseline for integration times of 100–300 s was improved by a factor ≈ 2, reducing the detection threshold by the same factor.

The availability of simultaneous 2.3 GHz observations with *TDRSA* for some of the sessions was of great assistance in correlating the 15 GHz data. The S/N of the 2.3 GHz *TDRSA*–ground data was considerably higher than the S/N of the 15 GHz data. The *TDRSA* clock parameters could be found from a fringe-search at 2.3 GHz and applied to correlation of 15 GHz data. This procedure was particularly effective when DSS 42 was observing, since it used the same clock as DSS 43. The 15 GHz data had sufficiently low S/N (near the detection threshold even for integrations for a coherence time across the entire passband) that a fringe-search without simultaneous 2.3 GHz data was much more difficult. Of the three observing sessions (1, 3, and 5) with no 2.3 GHz observations, fringes were detected on only two (1 and 5). An additional benefit of the 2.3 GHz data arose due to the residual fringe-rates at 2.3 and 15 GHz. The residual fringe-rate f due to uncertainties in the relative orientation of the source and the baseline in the equatorial plane is:

$$ f = \frac{\Omega v}{c} B_{eq} \cos \delta \cos (GHA - h)(\Delta h - \Delta GHA) , \qquad (1) $$

where Ω is the earth rotation rate, v is the observing frequency, c is the velocity of light, B_{eq} is the equatorial projection of the baseline length, δ is the source declination, GHA is the source hour angle at Greenwich (the difference between the Greenwich sidereal time and the right ascension of the source), h is the Greenwich hour angle of the baseline, and ΔGHA and Δh are the errors in GHA and h in the correlator model. There was initially a small coordinate system discrepancy (equal to the value of UT1–UTC, 5″ for this experiment) between the software used to produce the orbital ephemeris and the software used for the correlator model. This produced an error in the Greenwich sidereal time and gave a fringe-rate error of 300 mHz at 2.3 GHz (within the correlator window for a full-scan fringe-search) and 2 Hz at 15 GHz (outside the correlator window for such a search). Once fringes were found and tracked at 2.3 GHz, this error was detected and corrected.

Only the amplitudes of the correlation coefficients were saved from the fringe-fitting output. The signal-to-noise ratio (S/N) of the 15 GHz data was too low in all cases to enable useful source-structure constraints from closure phases. At 2.3 GHz, no closure phases were available, because there was never more than one ground station operating at one time.

Calibration of the 15 GHz data was hampered by antenna pointing problems and low S/N. The *TDRSA* antenna had not previously been used at 15 GHz in an open loop mode, and its pointing accuracy was very uncertain. The *TDRSA* design specification for open loop pointing was 0°15, approximately equal to the angle between the peak and the half-power point

of the 15 GHz beam. DSS 43 had previously been used only at frequencies of 8.4 GHz and below. System temperature measurements were made at DSS 43 before most scans (scans were 400 s long, with gaps of 7–20 minutes between scans), and antenna temperature measurements were typically made at DSS 43 once every 2 or 3 scans. For a few sources, these antenna temperature measurements varied by factors of 1.2–1.5, suggesting pointing errors as large as 0.32 beams (full width at half-maximum) for some scans. NRO is routinely used for observations at 85–120 GHz and had no difficulty pointing at 15 GHz.

The correlation coefficients were converted to correlated flux densities using the available system temperature and antenna temperature values (Cohen *et al.* 1975). A correction was made for the coherence loss determined for that baseline, epoch, and integration time (see § IV). The *TDRSA* G/T_{sys} value was determined from the three "crossing points" in the data. These crossing points occur when the *TDRSA*–DSS 43 and DSS 43–NRO projected baselines are equal, both in length and orientation (i.e., they have the same u-v values). Because the correlated flux densities on the two baselines must be equal at that moment, the relative sensitivities of *TDRSA* and NRO can be determined. The sensitivity of NRO was known from direct measurements during the experiment, allowing the sensitivity of *TDRSA* to be determined. The mean value for *TDRSA* from these three crossing points was 1.59×10^{-6} Jy^{-1} (consistent with 23% aperture efficiency and $T_{sys} = 1000$ K), with a spread of $\pm 5\%$. Due to the combination of this scatter with errors due to mispointing at DSS 43 (and perhaps *TDRSA*), we estimate that the absolute calibration of the 15 GHz data is uncertain by about 15%, with relative errors as large as 10% between scans on the same source (the data from scans with anomalously low antenna temperature measurements at DSS 43 were deleted). The measured correlated flux densities and source visibilities and model-fitting results are presented in § V. The 2.3 GHz data, limited to only one baseline, did not provide any crossing points. Therefore the *TDRSA* G/T_{sys} value from the second experiment (9.25×10^{-6} Jy^{-1}) was used. The 2.3 GHz results are presented in § V.

IV. COHERENCE

One of the primary goals of this experiment was a measurement of the coherence of the *TDRSA* system when used for VLBI at 15 GHz. VLBI observations at 15 GHz pose a much more stringent test of the entire system than observations at 2.3 GHz and approach the conditions of the highest observing frequency (22 GHz) planned for VSOP (Hirabayashi 1987) and RADIOASTRON (Kardashev and Slysh 1987). Because of the complexity of the oscillator chain (including phase transfer from the ground) and the potential importance of our results for future space VLBI missions, our coherence results are presented in considerably more detail than is typical for VLBI experiments.

The following procedure was used to calculate the coherence at 15 GHz. The 10 scans from sessions 6 and 7 (where phase measurements of the corrupted hydrogen maser were available) with the highest S/N were chosen. For these scans, the fringe phase was measured over short time intervals: 4, 10, or 20 s, depending on S/N. The scans were broken into segments of 60, 100, 120, 200, 300, and 340 s (only 340–350 s of each 400 s scan could be correlated, due to delays in tape synchronization at the correlator and to other technical reasons). The coherence of each segment was calculated as the

TABLE 3

15 GHz COHERENCE VALUES

Integration Time (s) (1)	TDRSA–Ground Mean Coherence (2)	Standard Deviation (3)	Error of Mean (4)	Ground Baseline Mean Coherence (5)	TDRSA Coherence (6)	Coherence Loss Ratio (15/2.3 GHz) (7)
20	0.970	...	0.010	0.997	0.972	5.6
40	0.950	...	0.010	0.993	0.954	5.1
60	0.933	0.065	0.010	0.988	0.939	2.3
100	0.902	0.055	0.010	0.980	0.912	2.8
120	0.892	0.065	0.011	0.976	0.904	2.2
200	0.851	0.077	0.017	0.961	0.870	3.1
300	0.786	0.063	0.020	0.959	0.806	2.6
340	0.761	0.093	0.029	0.948	0.787	2.7

ratio of the amplitude derived after removal of the best-fit linear phase rate (for that segment) to the "instantaneous" amplitude (that of the individual short intervals). One component of the amplitude reduction at the longer integration times arose from statistical phase measurement errors (i.e., due to limits S/N) for the short time intervals. A correction for this component was made, so as to give the true coherence loss. The coherence at 20 and 40 s was calculated using only those scans with 4 s phase measurements. Because the S/N of the data did not allow sampling the phase more frequently than 4 s intervals, the coherence loss on time scales of 4 s and shorter could not be determined.

The coherence results are presented in Tables 3 (15 GHz) and 4 (2.3 GHz). The 2.3 GHz coherence was calculated in a similar manner to the 15 GHz coherence, using eight scans from the TDRSA–Usuda baseline. In each table, the mean coherence is given in column (2) for eight different integration times, with the standard deviation of the coherence measurements in column (3). The estimated error on the mean coherence, calculated by dividing the standard deviation by the square root of the number of measured values, is in column (4). For integration times of 20 and 40 s, the standard deviation of the coherence values was dominated by uncertainties in the correction for low S/N, and it is therefore not listed. Column (5) in each table gives the coherence on ground-ground baselines: the errors are below 0.01 for all entries. The 2.3 GHz ground-ground coherence values are those from the second experiment. Column (6) gives a differenced coherence, which represents the estimated coherence of the complete TDRSA system at that observing frequency. For this calculation, it was assumed that the coherence loss (i.e., deviation of the coherence from 1.0) on the ground-ground baselines was equally divided between the two stations (troposphere and oscillator chain). Therefore, the coherence on the space-ground baselines was

corrected with the coherence on the ground-ground baselines to give the coherence of the TDRSA system:

$$C_{TDRSA} = \frac{C_{TDRSA-ground}}{\sqrt{C_{ground-ground}}} \,. \qquad (2)$$

C_{TDRSA} is the derived coherence of the TDRSA system, $C_{TDRSA-ground}$ is the coherence on TDRSA–ground baseline, and $C_{ground-ground}$ is the coherence on ground-ground baselines.

Figure 3 shows the dependence of the coherence at 15 GHz on integration time. The errors in the values plotted on the lowest curve (TDRSA–ground with uncorrected hydrogen maser, the situation for all data from sessions 1–5) are 0.05 or less. The apparent flattening of this curve for times larger than 100 s can be explained as follows: for times longer than the 100 s time constant of the phase-lock loop, the influence of the crystal oscillator drops.

Column (7) of Table 3 gives the ratio of the coherence loss of TDRSA at 15 GHz to that at 2.3 GHz. The coherence loss is 2.5–3.0 times larger at 15 GHz than at 2.3 GHz (the values at 20 and 40 s have large uncertainties). This ratio constrains the source of the coherence loss. Any errors in the orbit determination (i.e., errors in the knowledge of the TDRSA–radio source vector) would cause phase errors proportional to observing frequency and a coherence loss proportional (for small errors) to the square of the observing frequency. Orbit determination errors must therefore be a small component of the 2.3 GHz coherence loss (less than 10%). However, they could cause a significant portion of the 15 GHz coherence loss. Other possible sources of coherence loss are the spacecraft electronics and the LO link. The observed phase noise spectrum has a strong component proportional to $1/f$, where f is frequency. The on-board synthesizer chain was not designed

TABLE 4

2.3 GHz COHERENCE VALUES

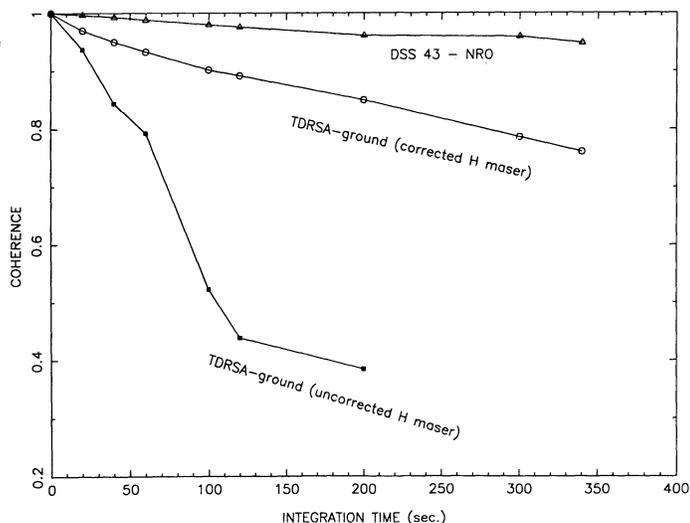| Integration Time (s) (1)	TDRSA–Ground Mean Coherence (2)	Standard Deviation (3)	Error of Mean (4)	Ground Baseline Mean Coherence (5)	TDRSA Coherence (6)
20	0.995	...	0.003	0.999	0.995
40	0.990	...	0.005	0.998	0.991
60	0.972	0.036	0.006	0.997	0.974
100	0.964	0.026	0.005	0.993	0.968
120	0.952	0.033	0.007	0.991	0.956
200	0.948	0.022	0.006	0.981	0.958
300	0.910	0.051	0.018	0.964	0.926
340	0.902	0.060	0.021	0.960	0.922

FIG. 3.—Measured coherence of 15 GHz VLBI data as a function of integration time. The upper curve shows the coherence on the DSS 43–NRO ground baseline. The middle curve shows the coherence on *TDRSA*–ground baselines when the corrupting effect of the crystal oscillator on the WSGT hydrogen maser was removed. The lower curve shows the *TDRSA*–ground coherence when this corrupting effect was not removed.

for high phase stability, and it would be expected to generate "frequency flicker noise" with a $1/f$ spectrum (J. Springett, private communication).

V. RESULTS

Eleven of the 22 sources observed at 15 GHz were detected on space-ground baselines. Table 5 presents information on baseline lengths, visibilities, and source structure models for those sources which were detected. Column (4) lists the "number of observations" for each source. This total is the sum over all baselines of the number of scans for which that source was detected. However, only one scan from the ground baseline (DSS 43–NRO) was counted, since all scans had very nearly the same u-v values. The estimated errors on the visibil-

TABLE 6
SOURCES NOT DETECTED ON *TDRSA*–GROUND BASELINES AT 15 GHz

Source Name	*TDRSA*–Ground Baseline Range ($D_\oplus$)	Total Flux Density (Jy)	Upper Limit to Correlated Flux Density (Jy)
0229+131	0.65–1.16	1.6	1.0
	1.21–1.50	...	0.6[a]
1127−145	0.99–1.13	1.6	1.3
1244−255	1.46	0.9	1.3
1519−273	1.50–1.57	1.2	1.5
1749+096	1.04–1.28	1.4	1.3
1921−293	1.48–1.52	5.5	1.4
2121+053	1.05–1.21	1.5	1.3
2216−038	0.98–1.19	...[b]	1.4
2230+114	1.17–1.22	...[b]	1.4
2318+049	0.80–1.23	1.3	1.0
	1.13–1.47	...	0.6[a]
2345−167	1.29–1.59	1.6	0.6

[a] The different upper limits for different baseline lengths represent the different sensitivities of the *TDRSA*–DSS 43 and *TDRSA*–NRO baselines.
[b] The total flux density of this source was not measured.

ities are 10%–15% of the listed values (the larger errors are for the weaker sources). The baseline lengths in Table 5 are on average smaller than those from the first two experiments. For sources south of declination 0°, *TDRSA*–NRO baselines are longer than *TDRSA*–DSS 43 baselines. Combined with the lower sensitivity of NRO (compared to that of DSS 43), this allowed fewer detections on the *TDRSA*–NRO baseline. In addition, the detection limit even on the *TDRSA*–DSS 43 baseline was higher than in the first two experiments because of the poorer sensitivity of both antennas. Table 6 presents upper limits for the sources which were not detected. There are three additional sources which were observed only in session 3 and are not included in either Table 5 or 6. In session 3 there were no simultaneous 2.3 GHz observations. None of the strongest sources (e.g., 3C 279) were observed in this session, and the uncorrected WSGT hydrogen maser gave poor coher-

TABLE 5
SOURCES DETECTED ON *TDRSA*–GROUND BASELINES AT 15 GHz

Source Name (1)	Baseline Range for Detection ($D_\oplus$) (2)	Position Angle of Longest Baseline (3)	Number of Observations[a] (4)	Total Source Flux Density (Jy) (5)	Visibility on Maximum Baseline (6)	Flux Density of Gaussian Model (Jy) (7)	Model FWHM[b] (mas) (8)
0221+067	0.58–1.32	51°	2	1.5	0.52	No model	...
0727−115	0.56–1.35	66	12	4.0	0.18	1.89	$0.14^{+0.06}_{-0.06}$
0823+033	0.58–1.26	−74	6	1.4	0.51	0.66	$0^{+0.10}$
1055+018	0.58–0.86	73	4	3.6	0.43	No model	...
3C 273[c]	0.58–1.33	−77	16	20	0.07	3.49	$0.14^{+0.06}_{-0.10}$
3C 279[d]	0.58–1.40	59	8	8.4	0.16	4.84	$0.14^{+0.07}_{-0.07}$
1334−127	0.57–1.63	−43	13	3.8	0.37	2.87	$0.10^{+0.05}_{-0.06}$
1510−089	0.54–1.18	−37	5	2.3	0.57	2.76	$0.12^{+0.03}_{-0.12}$
1730−130	0.53–1.14	18	6	4.1	0.18	1.88	$0.15^{+0.08}_{-0.07}$
2145+067	0.58–1.38	53	8	6.3	0.20	5.43	$0.16^{+0.03}_{-0.03}$
3C 446[e]	0.59–1.49	−85	9	5.1	0.23	1.98	$0.10^{+0.07}_{-0.10}$

[a] See the text for an explanation of this quantity.
[b] The errors represent 95% confidence limits for the size of a circular Gaussian model.
[c] 3C 273 = 1226+023.
[d] 3C 279 = 1253−055.
[e] 3C 446 = 2223−052.

ence. The combination of these factors prevented successful fringe-searching of the data from this session.

The fraction of sources detected on space-ground baselines at 15 GHz in this experiment, 50%, was considerably smaller than the fraction detected at 2.3 GHz in the second experiment, 96%. However, the detection thresholds were quite different at the two frequencies: 1.3 Jy at 15 GHz (0.6 Jy during sessions 6 and 7) versus 0.30–0.35 Jy at 2.3 GHz in the second experiment. If the detection threshold at 2.3 GHz in the second experiment had been 0.95 Jy (our average detection threshold at 15 GHz), 11 of 24 sources would have been detected on space-ground baselines, a fraction nearly identical to that at 15 GHz. Our 15 GHz data therefore are consistent with the hypothesis that the distributions of correlated flux densities on baselines of 1–2 Earth diameters are similar at 2.3 and 15 GHz. The same conclusion holds for the distribution of visibilities, since the total flux density distribution was very similar at the two frequencies.

Our 2.3 GHz data consisted of single baseline observations (*TDRSA* and one ground station) of 11 sources. Eight of these were detected. (This detection rate was lower than in the second experiment because the 2.3 GHz ground systems were less sensitive in this experiment and because sources were selected on the basis of their 15 GHz properties.) The baseline lengths and source visibilities for these eight sources are listed in Table 7. The errors of the visibilities are approximately $\pm 15\%$, with $\pm 25\%$ for the two weakest sources: $0823+033$ and $1519-273$. The baseline lengths and upper limits to the visibilities of the sources which were not detected are listed in Table 8. With only one baseline of data, which for half the sources occupies little more than a single point in the u-v plane, very little information about source structure can be determined. The low visibility of 3C 273 on the maximum baseline of $1.14\,D_{\oplus}$ reflects the strong resolution of the westward pointing jet with a baseline position angle of 75°. Five of the sources listed in Table 7 were observed in the second experiment at the same frequency and baseline. The agreement in correlated flux density is within the errors for 3C 279, $1334-127$, and $2345-167$. For $0727-115$ and $1519-273$, the correlated flux density is lower at the later epoch, by 1.0 ± 0.4 Jy and 0.5 ± 0.3 Jy, respectively. These decreases reflect similar decreases in the total flux densities.

Model fitting was performed for the 9 sources in Table 5 with the most 15 GHz data. Due to limited quantity and S/N of the data, only circular Gaussian models were used. The weighting of the data from the ground baseline was determined in the same way as described in Linfield *et al.* (1989). This

procedure avoided giving excess weights to the high S/N DSS 43–NRO data occupying a very limited region in the u-v plane.

After the best-fit circular Gaussian model was determined for each source, the data errors were uniformly scaled upward to bring the chi-squared agreement between model and data to 1.0 per degree of freedom. Then the size of the model was adjusted away from the best-fit value. For each trial value of the size, the flux density was allowed to vary so as to optimize the fit. However, the flux density was not allowed to exceed the sum of the measured single antenna flux density and the error on this measurement. As the size deviated from that of the best-fit model, the chi-squared difference between the model and data increased. The model errors quoted in Table 5 represent the range allowed at the 95% confidence level. These errors do not include the errors introduced by the assumption of a circular Gaussian brightness distribution. Our data are too sparse to adequately test this assumption in any of our sources.

For those nine sources in Table 5 with models, brightness temperatures can be derived (e.g., Lawrence *et al.* 1985). Table 9 lists the peak brightness temperatures (in the source rest frame) for all the Gaussian models. For six of the nine sources, the brightness temperature exceeds 10^{12} K, with values larger than 2×10^{12} K for three sources. The errors on the brightness temperatures are derived from the errors on the models (listed in Table 5) and neglect possible deviations from circular symmetry and Gaussian profiles.

TABLE 8

SOURCES NOT DETECTED ON *TDRSA*–GROUND BASELINES AT 2.3 GHz

Source Name	Baseline Range ($D_{\oplus}$)	Total Flux Density (Jy)	Upper Limit to Correlated Flux Density (Jy)
0221+067	1.12	0.9	0.45
3C 446	0.84–1.43	5.6	0.45
2318+049	0.79–1.22	1.2	0.45

TABLE 7

SOURCES DETECTED ON *TDRSA*–GROUND BASELINES AT 2.3 GHz

Source Name	Maximum Baseline ($D_{\oplus}$)	Total Flux Density (Jy)	Visibility on Maximum Baseline
0229+131	1.19	1.9	0.37
0727−115	1.65	2.9	0.20
0823+033	1.18	1.2	0.39
3C 273	1.14	36	0.03
3C 279	0.71	9.2	0.49
1334−127	1.23	2.8	0.32
1519−273	1.58	1.0	0.75
2345−167	1.59	2.9	0.19

TABLE 9

SOURCE BRIGHTNESS TEMPERATURES AT 15 GHz

Source Name	Peak Brightness Temperature[a] (10^{12} K)
0727−115	$0.54^{+0.8}_{-0.19}\,(1 + z)^{b}$
0823+033	$> 0.50\,(1 + z)^{b}$
3C 273	$1.14^{+6}_{-0.3}$
3C 279	$1.98^{+4}_{-0.7}$
1334−127	$2.27_{-0.9}$
1510−089	$1.55_{-0.65}$
1730−130	$0.87^{+1.6}_{-0.35}$
2145+067	$2.32^{+0.60}_{-0.32}$
3C 446	$2.40_{-1.1}$

[a] The errors listed correspond to the 95% confidence level for circular Gaussian models. Sources for which no positive error is given have a measured size which is consistent either with zero or a value too small to meaningfully constrain the brightness temperature.

[b] The redshift for this source is not known.

VI. SUMMARY

1. The technique of space VLBI, with phase transfer from a ground frequency standard to the orbiting antenna, has been demonstrated at 15 GHz, using a spacecraft which was not designed for VLBI.

2. Sources exist with greater than 1 Jy correlated flux density at 15 GHz on baselines of 1–2 Earth diameters. Future dedicated space VLBI missions with detection thresholds below 100 mJy will have many sources to observe in at least the 2.3–15 GHz range.

3. The distribution of brightness temperatures among extragalactic continuum sources at 15 GHz appears to extend up to at least 2×10^{12} K. The similar shape of the brightness temperature distributions at 2.3 and 15 GHz suggests that the sources are still optically thick at 15 GHz, consistent with the observed total flux density spectra of these objects.

REFERENCES

Broten, N. W., *et al.* 1967, *Science*, **156**, 1592.
Cohen, M. H., *et al.* 1975, *Ap. J.*, **201**, 249.
Hirabayashi, H. 1987, in *IAU Symposium 129, The Impact of VLBI on Astrophysics and Geophysics*, ed. M. J. Reid and J. M. Moran (Dordrecht: Reidel), p. 441.
Kardashev, N. S., and Slysh, V. I. 1987, in *IAU Symposium 129, The Impact of VLBI on Astrophysics and Geophysics*, ed. M. J. Reid and J. M. Moran (Dordrecht: Reidel), p. 443.
Lawrence, C. R., *et al.* 1985, *Ap. J.*, **296**, 458.

Levy, G. S., *et al.* 1986, *Science*, **234**, 187.
———. 1989, *Ap. J.*, **336**, 1098.
Linfield, R. P., *et al.* 1989, *Ap. J.*, **336**, 1105.
Morabito, D. D., Niell, A. E., Preston, R. A., Linfield, R. P., Wehrle, A. E., and Faulkner, J. 1986, *A.J.*, **91**, 1038.
Rogers, A. E. E., *et al.* 1983, *Science*, **219**, 51.
Sade, R. S., and Deerkoski, L. 1981, *Proc. AIAA/NASA Symposium on Space Tracking and Data Systems* (Washington, DC: GPO), pp. 77–81.

J. W. Barrett, B. F. Burke, S. R. Conner, M. B. Heflin, and J. Léhar: Department of Physics, Massachusetts Institute of Technology, Cambridge, MA 02139

R. J. Cappallo, A. E. E. Rogers, and A. R. Whitney: Haystack Observatory, Westford, MA 01886

S. J. DiNardo, C. D. Edwards, G. S. Levy, R. P. Linfield, L. J. Skjerve, L. R. Stavert, and J. S. Ulvestad: Jet Propulsion Laboratory, 4800 Oak Grove Drive, Pasadena, CA 91109

T. Hayashi, H. Hirabayashi, T. Nishimura, T. Takano, and T. Yamada: Institute for Space and Astronautical Science, 3-1-1 Yoshinoda, Sagimihara, Kanagawa 229, Japan

M. Inoue and M. Morimoto: Nobeyama Radio Observatory, Nobeyama 384-13, Japan

D. L. Jauncey: Division of Radiophysics, Commonwealth Scientific and Industrial Research Organization, Canberra, Australian Capital Territory 2601, Australia

M. J. Maher: Bendix Field Engineering Corporation, Suite 500, 10210 Greenbelt Road, Seabrook, MD 20706

C. H. Ottenhoff: TRW Space and Technology Group, Las Cruces, NM 88004

M. W. Pospieszalski: National Radio Astronomy Observatory, Edgemont Road, Charlottesville, VA 22901

J. Reynolds: Mount Stromlo Observatory, Australian National University, Canberra, Australian Capital Territory 2606, Australia

D. H. Roberts: Department of Physics, Brandeis University, Waltham, MA 02254